Check for updates

Received: 31 July 2024 | Accepted: 15 April 2025

DOI: 10.1002/nsg.70010

Near Surface Geophysics | EAGE European Association of Geoscientists & Engineers

ORIGINAL ARTICLE

Shear-wave tailored moveout corrections to improve multicomponent reflection seismic imaging

Samuel Zappalá | **Myrto Papadopoulou** | **Alireza Malehmir**

Department of Earth Sciences, Uppsala University, Uppsala, Sweden

Correspondence
Samuel Zappalá, Department of Earth Sciences, Uppsala University, Uppsala, Sweden.
Email: samuel.zappala@geo.uu.se

Funding information
Nationale Geologiske Undersøgelser for Danmark og Grønland

Abstract

Advancements in technologies and acquisition techniques in reflection seismology have increased the quantity of data that can be recorded in a single survey. The spreading of three-component (3C) recorders has resulted in multicomponent data acquisitions to be more cost-effective than single-component (1C) acquisitions, making 3C datasets more common. Therefore, the need for processing workflows aiming to enhance S-wave from P-wave-designed acquisitions is increasing. As part of a larger survey for geological carbon storage site investigations, a 1-km-long seismic profile was acquired near the city of Randers in Denmark and is considered in this study. The acquisition setup consisted of two vertical vibrating sources, operating every 10 m, recorded simultaneously from a 1C nodal array, 10 m spaced and a landstreamer system, equipped with 60 3C micro-electro-mechanical sensors in 2 m intervals. Analysis of the 3C data recorded from the landstreamer system shows PP-, PS- and SS-wavefield reflections from a shallow horizon nearly 50 m below the ground surface. Although the PP-wavefield data processing was straightforward, the SS-wavefield imaging was challenged by strong surface waves recorded in the data, thus requiring a tailored workflow for its processing. The workflow employs a reflection-picked moveout correction specifically designed on the observed reflections with respect to the data acquisition geometry. Results demonstrate that this tailored method is effective, yielding improved continuity of the SS-wavefield reflectivity with respect to the traditional normal moveout corrections. P- and S-wave interval velocity models are estimated in depth, and their ratio is computed to complement the geological interpretations of the shallow subsurface. Similar imaging scenarios can benefit from the proposed method to sharpen SS-wavefield reflections in stacked section.

KEYWORDS
data processing, imaging, near-surface, seismic, S-wave

INTRODUCTION

Between 2022 and 2023, a series of onshore 2D reflection seismic surveys were conducted in Denmark for carbon capture and storage (CCS) site investigations (Papadopoulou et al., 2023; Westgate et al., 2025; Zappalà, Malehmir, Papadopoulou, Westgate, et al., 2024). The data resulting from these studies have primarily been used to characterize the sites and assess their integrity for CO_2 injection. However, their size, diversity and quality also provide an excellent testbed for further research and for the evaluation of various imaging and processing workflows.

This is an open access article under the terms of the Creative Commons Attribution-NonCommercial License, which permits use, distribution and reproduction in any medium, provided the original work is properly cited and is not used for commercial purposes.
© 2025 The Author(s). *Near Surface Geophysics* published by John Wiley & Sons Ltd on behalf of European Association of Geoscientists and Engineers.

The data, generated by two vibrating sources operating every 10 m, were recorded using a dual-element recording system consisting of nodal recorders connected to geophones at 10 m spacing and micro-electromechanical sensors (MEMs) recorders spaced at 2 m and mounted on a landstreamer. The landstreamer recorders are 3C, which can provide a wealth of information regarding the subsurface properties, including S-wavefield data.

The S-waves recorded by the 3C receivers can be the result of two different wavefields. The first type is generated by the interaction of the P-wavefield with each interface in the subsurface, generating both transmitted and reflected P- and S-waves. The S-converted wavefield is referred to as PS-wavefield. The second type of S-wave is directly generated at the source position. This S-wave may also interact with subsurface interfaces, producing both transmitted and reflected P- and S-waves. This second type of S-wavefield is referred to here as SS-wavefield (Kearey et al., 2002).

Different studies have shown that S-waves can be generated from vertical sources depending on their coupling and shallow subsurface elastic properties such as seismic velocities of P- (V_P) and S-waves (V_S) (Brodic et al., 2018; Hardage, 2017; Hardage & Wagner, 2014a, 2014b; Miller & Pursey, 1954; Pugin & Yilmaz, 2017, 2019; Pugin et al., 2009). Miller and Pursey (1954) demonstrate that most of the energy of a vertical source produces an S-wavefield and only a minimum portion produces a P-wavefield. In particular, the ratio of V_P/V_S controls much of the energy that is transmitted into SV-wave from a vertical source (Pertuz & Malehmir, 2023a; Pugin & Yilmaz, 2017, 2019), whereas eventual anisotropy controls the energy leakage on the transverse component (Hardage, 2017). The advantages of S-wave seismic acquisitions have been highlighted by their increasing use over the last decade, especially for near-surface studies, such as engineering and hydrologic investigations (Bharadwaj et al., 2017; Brodic et al., 2018; Krawczyk, Polom, Malehmir, et al., 2013; Malehmir et al., 2016; Pugin et al., 2013) caused by their slower propagation velocities and consequent improved resolution with respect to P-wave data when similar frequencies are obtained (Burschil et al., 2015; Carr et al., 1998; Krawczyk, Polom, Beilecke, et al., 2013). Multicomponent studies enable improved understanding of wave propagation phenomena, wave conversion and inferred properties of the media like V_P, V_S and anisotropy (Carr et al., 1998; Krawczyk, Polom, Beilecke, et al., 2013) that complement the subsurface information retrieved from only vertical (V) component data (Hardage, 2015; Pugin & Yilmaz, 2017; Yilmaz, 2021). Nevertheless, S-wave data processing has different challenges compared to the known and well-established P-wave data processing workflows. In particular, surface waves show high amplitudes and similar velocities to the shallow SS-wavefield reflections with a partially overlapping frequency content. This dictates a dedicated processing flow, often differently tailored for different datasets, to reduce the impact of surface waves on the reflections (Burschil & Buness, 2020; Van Zanen, 2004; Wadas et al., 2016), unless the presence of a high-velocity top layer suppresses surface wave generation (Inazaki, 2004; Polom et al., 2010). This study proposes a workflow to obtain SS-wavefield stacked sections using a reflection-picked moveout correction, which addresses long wavelength statics and flattens reflection responses in common midpoints (CMP) gathers. We focus on seismic data from a 1-km long section of profile 13 (Figure 1), from the survey conducted in the Gassum area (Westgate et al., 2025) near the city of Randers, chosen for its favourable weather and smooth road geometry, ensuring high data quality and minimal artefacts. The aim is to effectively utilize the acquired S-wavefield components for interpreting shallow subsurface information. In addition, velocity analyses of P- and S-wavefields are conducted to compare results and complement the geological interpretation. The methods developed in this study will benefit similar near-surface applications by improving imaging in cases where target reflections are partially masked by surface waves or other coherent noise.

Seismic data acquisition and analysis

Regional studies and borehole data (Energi Randers Vand A/S, 2007; Miljø- og Fødevareministeriet, 2020; Naturstyrelsen, 2014) show that the shallow subsurface in the area comprises 30–40 m of alternating quaternary sand and clay layers overlaying a discontinuous 10 m-thick layer of pre-quaternary clays from Paleocene epoch. Below these, limestones from Danian age corresponding to the top part of the Chalk Group (Lieberkind et al., 1982; Surlyk et al., 2006) are present (Figure 2). Most of the boreholes in the area are from the 1960s and 1970s with available data restricted to lithological information and water table depth. The available boreholes are projected on a geological section running parallel to the profile (Figure 1a) and extending towards the south to cross the deepest borehole available in the vicinity (Figure 2). Considering the local stratigraphy, the strongest expected near-surface reflection is the top of the Danian limestones as it has a good continuity and the strongest impedance contrast in the area (Papadopoulou et al., 2023; Westgate et al., 2025; Zappalá, Malehmir, Papadopoulou, Gregersen, et al., 2024). Contrariwise, sands and clays from the alternating quaternary layers are expected to share similar density and velocity values, with a typical density of 1.6–2.6 g/cm^3 for clays and 1.7–2.3 g/cm^3 for sands and a velocity of 1100–2500 m/s for clays and 1500–2000 m/s for sands (Kearey et al., 2002). Thus, their impedance contrasts

18730604, 0, Downloaded from https://onlinelibrary.wiley.com/doi/10.1002/nsg.70010 by Samuel Zappalá - Uppsala Universitet , Wiley Online Library on [08/05/2025]. See the Terms and Conditions (https://onlinelibrary.wiley.com/terms-and-conditions) on Wiley Online Library for rules of use; OA articles are governed by the applicable Creative Commons License

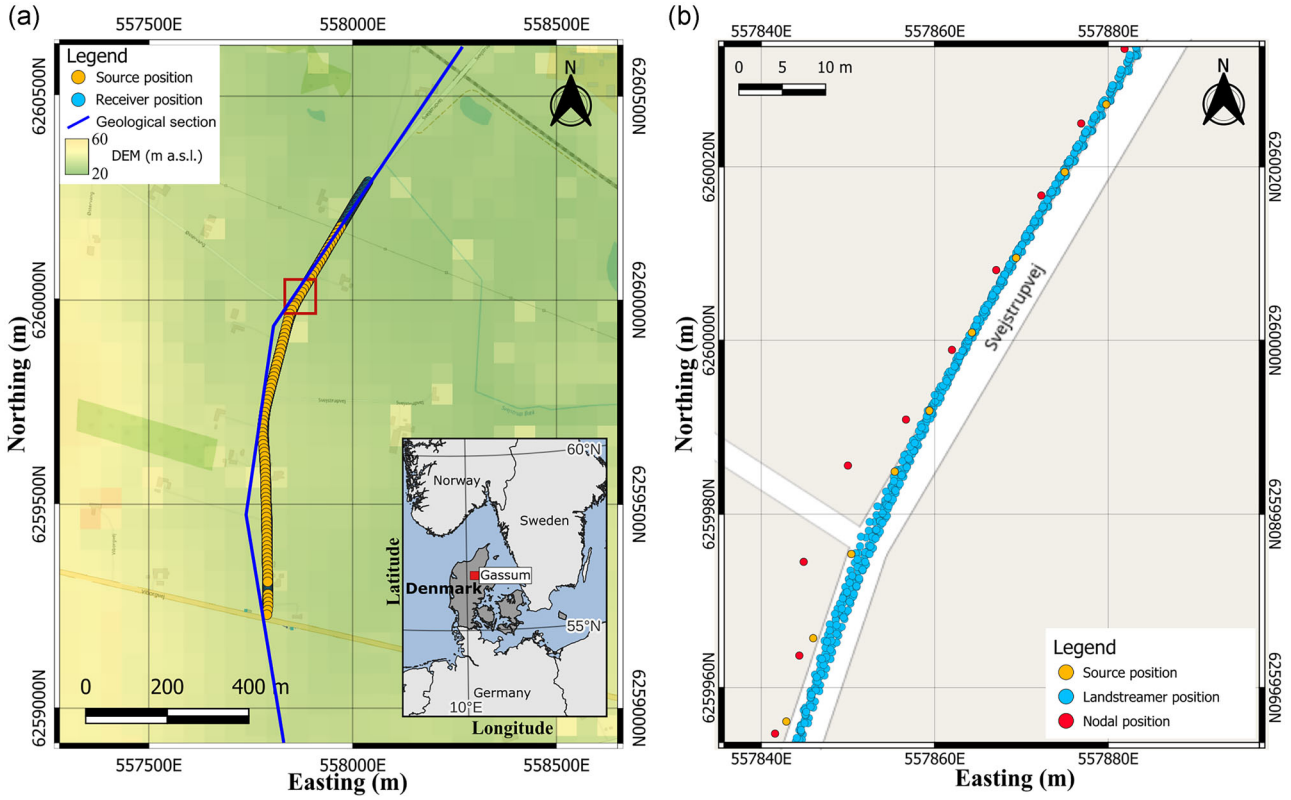

Figure 1 (a) Acquisition map of a portion of profile 13, the focus of this study. (b) Close-up portion (red rectangle in (a)) of the profile exemplified in this study, yellow circles are source positions, blue circles are the position of the landstreamer receivers and red circles are the position of the nodal receivers. Note that the geological section (blue line) continues outside the displayed area.

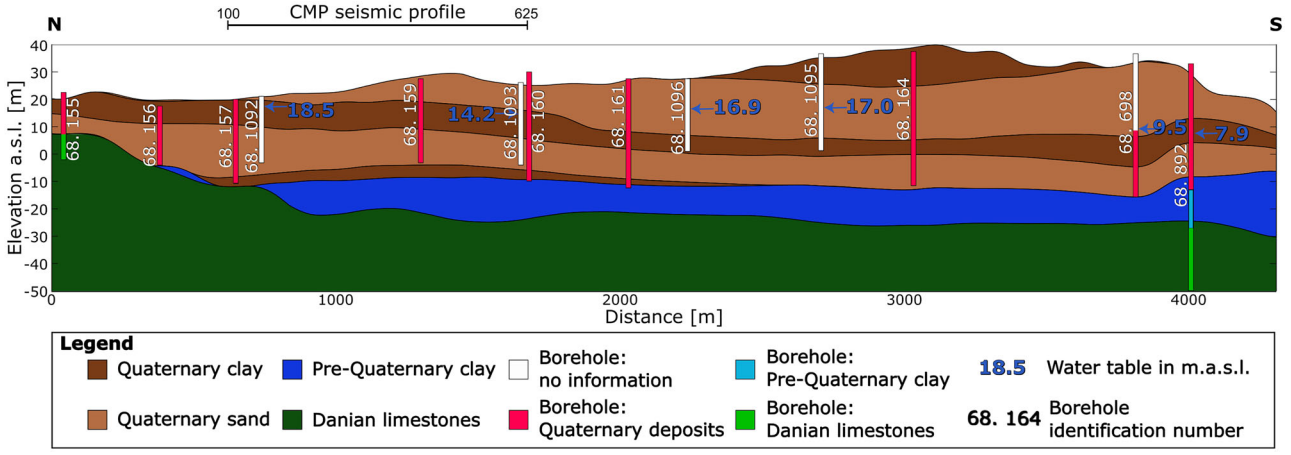

Figure 2 A simplified geological cross section along the acquired line (solid line in Figure 1a), reproduced from the geological interpretation of Energi Randers Vand A/S (2007), Miljø- og Fødevareministeriet (2020) and Naturstyrelsen (2014) after GeoAtlas (2024). The relative seismic profile location is indicated by the black line 'common midpoints (CMP) seismic profile', whereas the shown geological section covers a larger area. Boreholes available within 100 m perpendicular distance from the profile are projected onto the cross-section.

are expected to be low. The pre-quaternary clay unit appears to have poor lateral continuity that makes its detection difficult by seismic methods.

The acquisition setup used during this survey was modified following a survey conducted by Malehmir et al. (2022). Two 12 *t* seismic vibrator trucks were used as the seismic vertical source and operated in a phase lock mode to avoid distortion and anti-phase vibration. The source configuration was kept the same as previous studies (e.g., Malehmir et al., 2022; Papadopoulou et al., 2023; Westgate et al., 2025) to ensure that the two sources produced constructive interference, and a

18730604, 0, Downloaded from https://onlinelibrary.wiley.com/doi/10.1002/nsg.70010 by Samuel Zappalá - Uppsala Universitet , Wiley Online Library on [08/05/2025]. See the Terms and Conditions (https://onlinelibrary.wiley.com/terms-and-conditions) on Wiley Online Library for rules of use; OA articles are governed by the applicable Creative Commons License

spacing of 10 m was kept between each shot point. At each shot point, a linear 10–140 Hz sweep with a duration of 18 s was generated and then repeated three times to improve the signal-to-noise ratio (S/N) after vertically stacking shots from the same location. A 120-m-long landstreamer was towed at the back of the second source truck, equipped with 60 3C MEMs (0–800 Hz) 2-m-spaced recorders. The total recording time was 25 s using a sampling rate of 1 ms. The two seismic vibrator trucks were positioned one after the other with a distance of approximately 7 m between the plates. The middle point between the plates was considered the source point with the first sensor of the landstreamer placed approximately 10 m behind it, resulting in a maximum offset of approximately 130 m. The landstreamer was dragged with an end-on spread geometry along a road for approximately 1 km (Figure 1a). Parallel to the road, a nodal array of 10-Hz vertical geophones with 10 m spacing and 2 ms sampling rate was also deployed.

Specific for this study, differential global positioning system (DGPS) coordinates were acquired with a decimetre accuracy for every 20th landstreamer recorder and for each shot point, meaning four DGPS measurements per shot corresponding to recorders 1, 21, 41 and 60. The coordinates were interpolated to cover all receiver locations, whereas the source position was extrapolated 10 m in front of the first unit (recorder 1) considering the landstreamer direction (Figure 1b). These measurements, physically and time demanding, differ from what has been done in the rest of the surveys (as detailed by Papadopoulou et al. (2023)) increasing the accuracy of the landstreamer coordinates and for the purpose of examining S-wavefield reflection sensitivities to the SS-wave static corrections.

Seismic raw data

The recorded data show variable quality among the shot gathers and different components. In Figure 3a, the *V* component shows strong first arrivals and continuous shallow reflections down to 300–400 ms. On the other hand, the horizontal (*H*) components, both radial (HR, Figure 3b) and transverse (HT, Figure 3c), show less continuity for the first arrivals but two strong and continuous reflections are visible at 200 and 400 ms. The HR component shows lower S/N compared to the HT component, resulting in a decreased continuity of the reflections. Furthermore, the HR component appears more sensitive to cultural noise (Figure 3b,c). Similar effects on HR and HT components are observed also in other studies (Hardage & Wagner, 2014a, 2014b; Pertuz & Malehmir, 2023b; Pugin & Yilmaz, 2017, 2019). Pertuz and Malehmir (2023a) after acquiring and analysing a 9C dataset show in their results that the combinations of *V*-source-HT-receivers and HT-source-HT-receivers are the optimal orientations for S-wavefield imaging in highly sensitive clays, showing an improved quality from HT to HR components. Another example of a 9C dataset from Pugin and Yilmaz (2019) shows that the best quality for S-wavefield imaging over normally consolidated materials (e.g., soils) is given by the combinations of HT-source-HT-receivers, but they do not analyse a favourable combination for a *V*-source. Considering the variable results in literature (e.g., Macrides & Kelamis, 2000; Pertuz & Malehmir, 2023a; Pugin &Yilmaz, 2019; Pugin et al., 2009) and the overall higher quality of the HT component data in our study, in this work only the HT component is used for the SS-wavefield reflection data processing, and the HR component dataset is disregarded.

The recorded surface waves are strong in all the three components, with velocities ranging between 200 and 400 m/s. Below 600 ms only a few reflections with low continuity and variable signal amplitude are visible in the shot gathers.

We identified three main reflections (Figure 3). The shallowest one is more continuous in the *V* component, with its apex around 100 ms and an RMS velocity of approximately 1400 m/s. The second reflection, notable in all components, shows higher continuity in the HT component, peaking at around 200 ms and an RMS velocity of 750–850 m/s. The deepest reflection is more pronounced in the horizontal components, with its apex at around 400 ms and a velocity of 300–400 m/s. Hodograms were computed for each reflection (Figure 3d–f) to analyse particle motion. Results indicate that the shallowest reflection, referred to as PP, is P-wave in nature, whereas the second reflection, visible in both *V* and *H* components, is likely a converted-wave reflection (PS). The latest reflection, primarily seen in the HT component, indicates a pure shear nature (SS). Considering the observed velocities, these reflections represent different wave-modes, PP, PS and SS, generated from a single reflector and thus requiring distinct processing flows to obtain the respective image (Table 1).

METHODOLOGY

P-wave reflection data processing

To obtain the P-wave stacked section, the *V* component data were processed according to the flow described in Table 1. Different steps and values were evaluated before defining the processing flow. After deconvolving the raw data with the theoretical sweep using the frequency-domain sweep deconvolution method (Brittle et al., 2001) and vertically stacking the repeated shot records performed at the same shot location, a match filter was computed and then applied to the data to sharpen the reflections as shown in Zappalá, Malehmir, Papadopoulou, Gregersen et al. (2024). First breaks

18730604, 0, Downloaded from https://onlinelibrary.wiley.com/doi/10.1002/nsg.70010 by Samuel Zappalá - Uppsala Universitet , Wiley Online Library on [08/05/2025]. See the Terms and Conditions (https://onlinelibrary.wiley.com/terms-and-conditions) on Wiley Online Library for rules of use; OA articles are governed by the applicable Creative Commons License

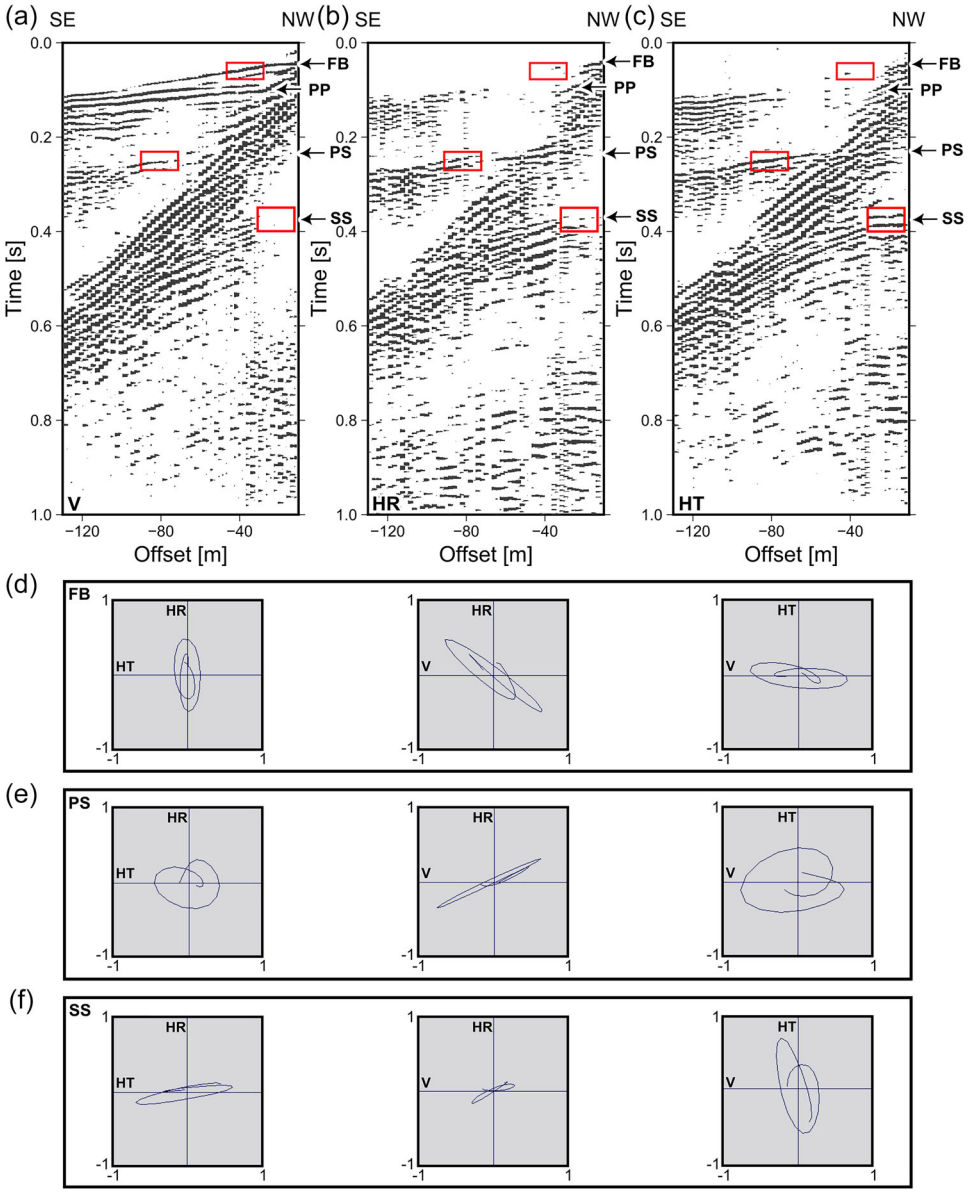

Figure 3 An example of a shot gather from the landstreamer data shown for (a) *V* component, (b) HR component and (c) HT component. Hodograms are calculated from the red boxes shown in (a–c) for (d) the first-break arrivals (FB), (e) the interpreted PS reflection and (f) the SS reflection. To enhance visualization, automatic gain control (AGC, 500 ms) and a bandpass filter (30–40–90–110 Hz) were applied to the data after vertically stacking the repeated deconvolved shot records.

were picked to enable the near-surface velocity model estimation for refraction static corrections. CMP were designed at every 2 m to achieve a reasonable fold coverage while maintaining an improved lateral resolution. A correction to a floating datum is applied to reduce elevation discrepancies in the data. A bandpass filter (35–50–140–170 Hz) and a swell noise attenuation filter were applied to attenuate the surface waves showing frequencies up to 40 Hz. Spherical divergence corrections were applied prior to the swell noise attenuation filter to compensate for geometrical spreading effects. Ringing effects of two different cycles of 14 and 20 ms were detected in the data, and Wiener-gapped deconvolution was applied to attenuate them using an application window of 50 and 150 ms, respectively. Constant velocity stack analysis was performed to calculate a normal moveout (NMO) RMS velocity model looped with one run of surface-consistent residual static corrections. The resulting velocity for the PP-wavefield reflection ranges between 1300 and 1500 m/s. After stacking the CMP gathers with an NMO stretch mute of 60%, the data were corrected to their final datum. An additional bandpass frequency filter and an FX-deconvolution were applied after stacking to reduce artefacts and increase the coherency of the signal. The resulting PP-wavefield unmigrated stacked section appears clean with a continuous pattern of reflections between 100 and 200 ms (Figure 4).

18730604, 0, Downloaded from https://onlinelibrary.wiley.com/doi/10.1002/nsg.70010 by Samuel Zappalá - Uppsala Universitet , Wiley Online Library on [08/05/2025]. See the Terms and Conditions (https://onlinelibrary.wiley.com/terms-and-conditions) on Wiley Online Library for rules of use; OA articles are governed by the applicable Creative Commons License

Table 1 Reflection processing steps applied for the PP- and SS-wavefield processing.

	PP-wavefield processing	SS-wavefield processing
1	Read SEGD data, convert to SEGY and assign geometry	
2	Deconvolution with the theoretical sweep	
3	Vertical shot stacking (three shot records)	
4	Keep only vertical component traces	Keep only horizontal transverse component traces
5	Match filter application	
6	First-break picking	–
7	Trace editing	
8	Geometry setup (CMP spacing 2 m)	
9	Elevation static corrections to a floating datum (30 m, 1400 m/s)	
10	Frequency bandpass filter (35–50–140–170 Hz)	
11	Spherical divergence correction	
12	Swell noise attenuation	Median horizontal filter (290 m/s)
13	Apply AGC (500 ms)	
14	Wiener-gapped deconvolution (window 150 ms, gap 20 ms)	
15	Wiener-gapped deconvolution (window 50 ms, gap 14 ms)	
16	Remove AGC (500 ms)	
17	Refraction static corrections (rms 1.9 ms)	AGC (1000 ms)
18	Constant velocity stack analysis	
19	Surface-consistent residual static corrections (one run)	Reflection picked moveout corrections (Pick arrival times at desired reflection)
20	AGC (300 ms)	Reflection picked moveout corrections (extrapolate hyperbola apex at each CMP)
21	NMO corrections (60% stretch mute)	Reflection picked moveout corrections (correct each trace to the hyperbola apex)
22	Stack	
23	Elevation static corrections to final datum (30 m, 1400 m/s)	
24	Frequency bandpass filter (15–40–140–170 Hz)	
25	FX-deconvolution	
26	Export for plotting	

Abbreviations: AGC, automatic gain control; CMP, common midpoint; NMO, normal moveout.

Results from the PS-wavefield did not provide quality sections and therefore these data are not presented nor further discussed in this paper.

SS-wavefield reflection processing

To obtain the SS-wavefield stacked section, HT components were processed. Although the SS-wave reflection appears strong in the shot gathers, the similarity in velocity and arrival times of its hyperbola limbs with the surface waves (Figure 3c) together with the low CMP fold coverage made its imaging challenging. The following methods were tested to discriminate the surface waves from the desired SS-wavefield reflection, but their similarity resulted too strong to properly separate them as already seen in literature (e.g., Van Zanen, 2004). Low frequencies were removed up to 40 Hz with a bandpass filter to reduce the surface waves component. This partially worked but surface waves were still strongly present at the same frequency range of the reflection. A median horizontal filter targeting the main velocities shown from the surface waves was applied but the incoherency of the surface waves velocities and the different higher modes resulted on a poor effect of this filter. FK-filtering was applied to remove the signal related to surface waves but any selected spectral window able to affect the surface waves resulted in a strong reduction of the SS-wavefield reflection continuity. The swell noise attenuation filter showed good results on reducing the surface waves for the P-wave processing, but it removed part of the SS-wavefield reflection as well. Surgical mute was applied to remove part of the surface waves above the SS-wavefield reflection, but it was not able to solve the separation problem of the two wave types. Furthermore, the SS-wavefield imaging is

18730604, 0, Downloaded from https://onlinelibrary.wiley.com/doi/10.1002/nsg.70010 by Samuel Zappalá - Uppsala Universitet , Wiley Online Library on [08/05/2025]. See the Terms and Conditions (https://onlinelibrary.wiley.com/terms-and-conditions) on Wiley Online Library for rules of use; OA articles are governed by the applicable Creative Commons License

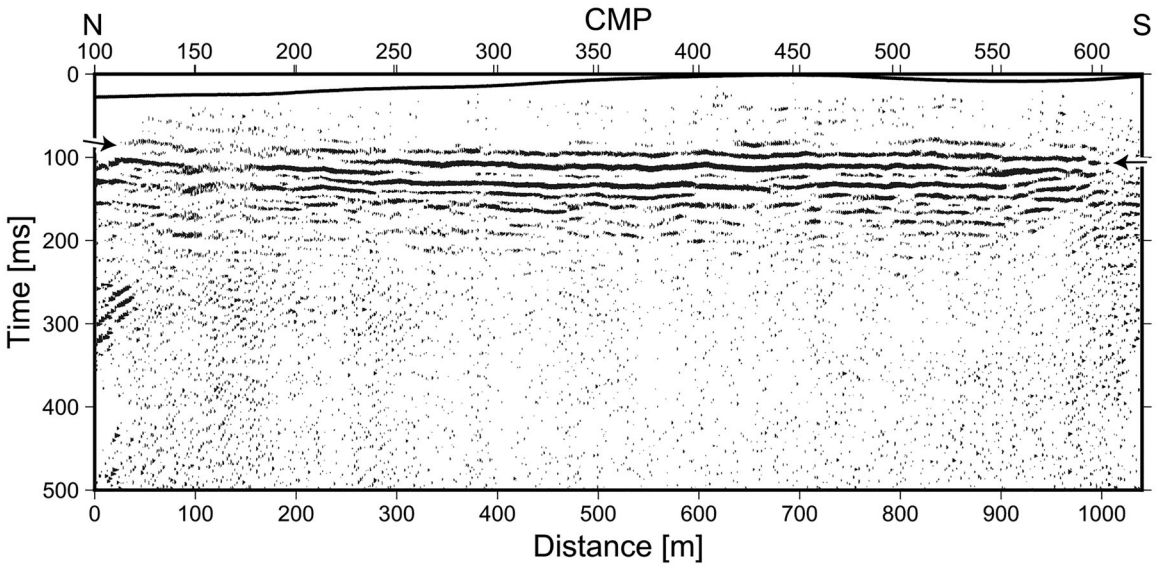

Figure 4 Unmigrated stacked section of the *V* component data using the PP-wavefield processing workflow. The top black line represents the surface elevation converted to time. Note the reflectivity pattern marked using black arrows at around 100 ms. CMP, common midpoint.

more sensitive to subsurface discontinuities and to out-of-plane reflections because of the slower V_S compared to the V_P (Carr et al., 1998; Krawczyk, Polom, Beilecke, et al., 2013), resulting in a more complicated wavefield composition.

Thus, a processing workflow was developed and tailored for the HT component data (Table 1), with most of the steps similar to the PP-wavefield processing workflow. For the HT component data, the swell noise attenuation filter was replaced with a less data-affecting median horizontal filter (290 m/s). To address surface waves contamination and flatten reflection hyperbolas before stacking, the traditional NMO corrections were replaced with an alternative approach, referred to here as reflection-picked moveout corrections (Figure 5). This method involves manually identifying the desired reflection, which allows for a direct computation of the moveout corrections based on the picked reflection, effectively distinguishing reflections from surface waves and reducing reliance on coherency methods (e.g., RMS velocity estimation) that may not differentiate between them. An additional advantage of this process is the intrinsic compensation for static corrections. The process consists of six steps (Figure 5): (1) pick the reflection time on each receiver trace (x, t) in shot gather domain, where possible; (2) remove the receiver traces that have poor quality; (3) sort the picked data in CMP gather domain and estimate the best fitting V_{rms} velocity hyperbola for the picked reflection events as a function of offset; (4) extrapolate the fitted hyperbola to the picked traveltimes to estimate the reflection apex (x_0, t_0) for each CMP gather; (5) compute the difference between the picked time of the reflection (x, t) and the estimated apex time (x_0, t_0) for traces at non-zero offset, yielding an improved reflection moveout correction; (6) shift each receiver trace by the computed corrections to flatten reflections at their apex (t_0) and stack the data for each CMP gather. These steps assume a horizontally layered subsurface, consistent with the expected geology in the area (Westgate et al., 2025).

To estimate the time for the apex of the hyperbola (Figure 5, Step 4), the following mathematical expression derived from the hyperbola equation is used:

$$t_0 = \sqrt{t^2 - \frac{x^2}{V_{rms}^2}} \quad (1)$$

In Equation (1), t is the reflection time at a certain offset x (Figure 5, Step 1), t_0 is the time of the hyperbola apex (Figure 5, Step 4), and V_{rms} is the corresponding root mean square velocity (Figure 5, Step 3). Both t and x are known from the data, whereas V_{rms} can be estimated by fitting a theoretical hyperbola to the picked traveltimes. Therefore, the solution of Equation (1) provides t_0 (Figure 5, Step 4), and the moveout to apply to each trace will correspond to the difference between t_0 and t of the corresponding traces picked in Step 1 (Figure 5, Step 5). After applying these corrections, the picked reflection in the CMP gathers will flatten at the estimated hyperbola's apex (Figure 5, Step 6).

If the data contain the zero-offset traces (x_0), the t_0 time can be directly measured from the hyperbola's apex (Figure 5, Step 4), and therefore, Steps 3 and 4 can be skipped. Step 2 is not essential in the case of data with good S/N but will remove traces where the reflection signal shows poor quality in case of a lower S/N. To assess the effectiveness of the method on real data, Figure 6 shows a flattened SS-wavefield reflection after NMO corrections for a few CMP gath-

18730604, 0, Downloaded from https://onlinelibrary.wiley.com/doi/10.1002/nsg.70010 by Samuel Zappalá - Uppsala Universitet , Wiley Online Library on [08/05/2025]. See the Terms and Conditions (https://onlinelibrary.wiley.com/terms-and-conditions) on Wiley Online Library for rules of use; OA articles are governed by the applicable Creative Commons License

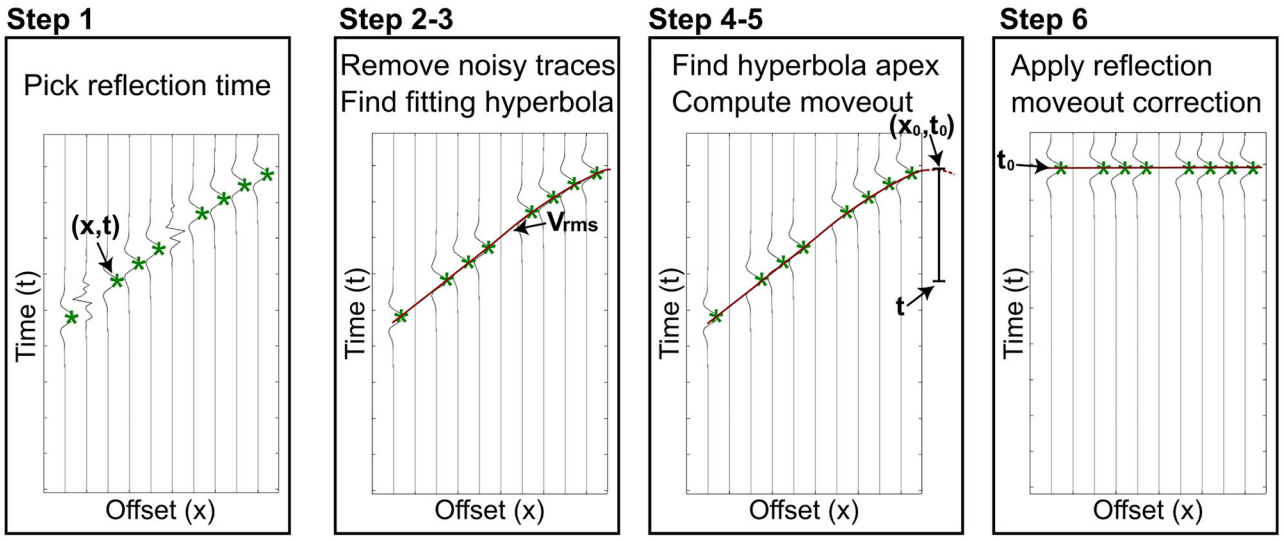

Figure 5 Example of the SS-wavefield reflection-picked moveout corrections process on synthetic data. In Step 1, the reflection is manually picked (x, t). In Steps 2 and 3, the noisy traces are removed, and a theoretical hyperbola of V_{rms} velocity is fitted with the picked reflection. Steps 4 and 5 involve estimating the hyperbola apex (x_0, t_0) and the moveout for each trace. In Step 6, the reflection is flattened after the moveout corrections.

ers as compared with the reflection-picked moveout corrections. The SS-wavefield reflection after NMO corrections can hardly be identified (Figure 6a), but after the application of the proposed reflection-picked moveout corrections (Figure 6b), its continuity improves. The reflection-picked moveout corrections developed here inherently compensate also for refraction and residual static corrections. Thus, the resulting section is superior compared to the one computed from standard normal moveout-corrected gathers. This is not surprising given the large time delays for SS-wavefield refraction static corrections as opposed to PP-wavefield refraction static corrections. A few attempts to utilize the PP-wavefield static corrections were made by multiplying them by a factor of two, three and four but this did not provide quality sections as compared to the method shown here suggesting a high variability of the V_P/V_S ratio for this case.

The unmigrated stacked section using an NMO velocity of around 350 m/s estimated from constant velocity stack analysis shows a reflection at approximately 350 ms (Figure 7a). The reflection is visible, but it is of a poor quality for interpretation. On the other hand, the unmigrated stacked section resulting from the proposed workflow (Figure 7b) shows improved reflection continuity and is of easier interpretation for the selected horizon.

P- and S-wave velocity estimations

To validate and complement the seismic section, different approaches to estimate V_P and V_S were applied. Figure 8a presents the RMS velocities at the reflection location (approximately −20 m elevation a.s.l.) computed from the fitted theoretical hyperbolas estimated in Step 3 of the reflection-picked moveout corrections (Figure 5), which vary between 300 and 500 m/s and show an overall increasing trend towards the southern portion of the section.

To estimate the V_P/V_S ratio (Figure 8b), the PP- and SS-wavefield reflections were picked in their corresponding unmigrated stacked sections in time (Figures 4 and 7b), and the obtained traveltimes were divided assuming they are from the same horizon that corresponds to the bottom of the first seismic layer. The resulting ratio (Figure 8b), an average V_P/V_s ratio down to the reflection depth (approximately −20 m elevation), is approximately 4 on the northern side of the profile and progressively decreases towards the south until a value of approximately 3 is observed. Portions of the SS-wavefield reflection are difficult to pick with accuracy, and therefore, the corresponding portions of the V_P/V_S ratio profile could not be calculated, leading to the gaps in Figure 8b.

A P-wave tomographic velocity model derived from the first breaks was computed from the nodal data that were acquired contemporarily with the landstreamer data. Using this different dataset offers two advantages: (1) The nodal array provides higher offsets and fold coverage with respect to the landstreamer array, ensuring inversion stability and deeper ray penetration, and (2) the independence of the two datasets. A diving-wave finite-difference-based code (Tryggvason et al., 2002) was employed to compute traveltime tomography from the picked first breaks in the nodal data. The code

18730604, 0, Downloaded from https://onlinelibrary.wiley.com/doi/10.1002/nsg.70010 by Samuel Zappalá - Uppsala Universitet , Wiley Online Library on [08/05/2025]. See the Terms and Conditions (https://onlinelibrary.wiley.com/terms-and-conditions) on Wiley Online Library for rules of use; OA articles are governed by the applicable Creative Commons License

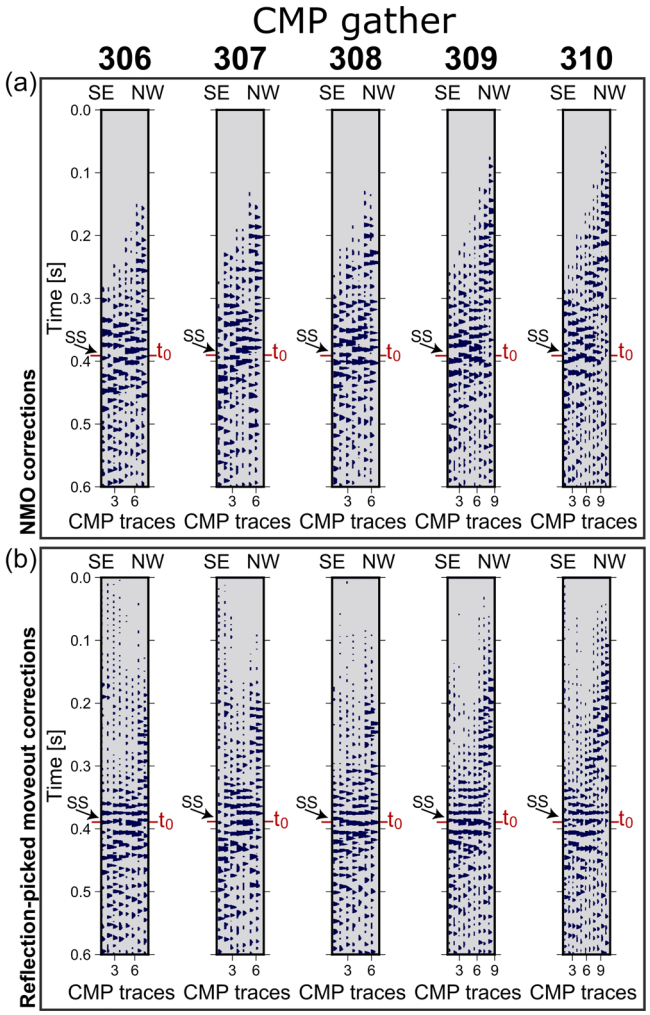

Figure 6 Common midpoints (CMP) gathers after (a) traditional normal moveout corrections and (b) the proposed reflection-picked moveout corrections. The estimated time of the hyperbola's apex is shown on the gathers as t_0. Note the improved alignment of the SS-wavefield reflection at t_0 in the reflection-picked moveout corrections method compared with the traditional normal moveout-based corrections.

applies 3D equations for the ray path computation, and results are constrained to a 2D straight line parallel to the profile. Picks up to 1.5 km of offset guaranteed a ray penetration down to 100 m below sea level. The resulting velocities range from 800 m/s in the shallowest portion to 2700 m/s at the bottom of the model, showing high velocity contrasts at around 15 and −15 m elevations a.s.l. and a rms error of 4 ms (Figure 8c down to −10 m elevation a.s.l.).

Leveraging the strong surface waves recorded in the data and the 2 m landstreamer spatial sampling that allows complete recovery of low-velocity waves, a V_S model was estimated. The *V* component data recorded the most coherent surface waves (Figure 3a), likely due to the vertical source, and thus were used to estimate the dispersion curves. An automatic picking of the fundamental mode (Papadopoulou et al., 2021) was applied and followed by a manual correction to ensure the quality of the picks. Higher modes were excluded due to low coherency. The V_S model was computed using a laterally constrained inversion (Socco et al., 2009) with 546 1D starting models spaced 22 m apart. The model consisted of seven layers, six with a thickness of 5 m and a V_S of 300 m/s, and the deepest one with a thickness of 10 m and a V_S of 500 m/s, for a total model depth of 40 m. The initial Poisson's ratio was approximated as 0.25, in agreement with the expected V_P and V_S observed in the data. Resulting velocities ranged from 150 m/s in the shallowest part of the model to 700 m/s at its bottom with an error of 4.8% of the observed velocities, showing a general trend of increasing velocity from the north towards the south (Figure 8d). These results should not be directly compared to the ones shown in Figure 8a due to the different velocity types and depths involved. With respect to the V_P model (Figure 8c), similar structures are visible in the shallowest levels (first 20 m) and mainly in the southern portion of the profile. However, notable differences exist, particularly on the northern side, between CMP 150 and 300, where a low-velocity zone is present in the V_S but absent in the V_P model. The limited wavelength band of the dispersion curves restricted the model reconstruction to a depth of 40 m (−10 m elevation), preventing V_S estimation at greater depths, including the identified horizon depth.

The V_P/V_S ratio obtained by dividing the traveltime tomography and the surface wave inversion is shown in Figure 8e. The result is independent from the V_P/V_S ratio estimated from the stacked sections (Figure 8b), as in this case, the V_P/V_S ratio estimated from 2D models varies both in horizontal space and as a function of depth, and therefore, they are not directly comparable. The V_P/V_S ratio values, ranging from 1.5 to 4.5, show an overall increasing trend towards the south similar to the result of Figure 8b. We observe high V_P/V_S ratio values (>3) at around 5–10 m elevation almost everywhere in the model, whereas a high V_P/V_S ratio (>4) anomaly is detected in the north side of the profile between CMP 150 and 200 at a depth between sea level to almost the surface, and the model from Figure 8b shows similar trends. It is important to note that due to the limited depth of the V_S model, because of the shallow penetration of the surface waves, the V_P/V_S ratio in Figure 8e reaches a depth of approximately −10 m elevation and is more reliable at the depths above sea level, whereas the V_P/V_S ratio from the stacked sections (Figure 8b) corresponds to an average of the column above the depth of the reflection at around −20 m elevation. The unmigrated stacked section of the SS-wavefield is converted to depth using an average depth velocity (Socco et al., 2017) of the top 30 m from the V_S model (Figure 8d) and smoothly linearly increasing down to 50 m of depth. Even if poorly accurate, this method allows an overall comparison with the depth velocity models and an estimation of the horizon depth at around 50 m.

18730604, 0, Downloaded from https://onlinelibrary.wiley.com/doi/10.1002/nsg.70010 by Samuel Zappalá - Uppsala Universitet , Wiley Online Library on [08/05/2025]. See the Terms and Conditions (https://onlinelibrary.wiley.com/terms-and-conditions) on Wiley Online Library for rules of use; OA articles are governed by the applicable Creative Commons License

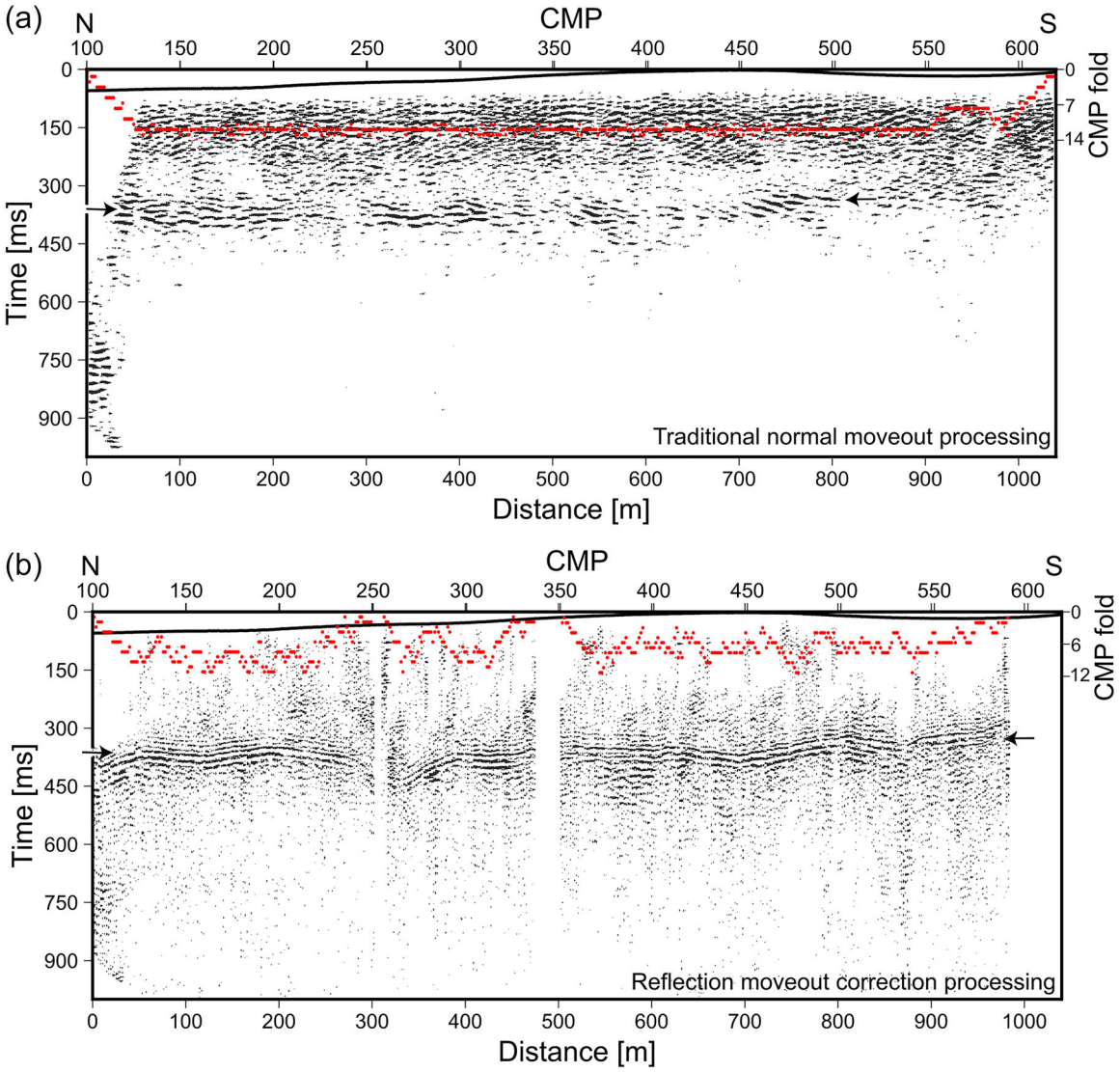

Figure 7 Unmigrated stacked section of the SS-wavefield from the HT component data after (a) applying normal moveout corrections and (b) implementing the reflection-picked moveout corrections developed in this study. The red dots indicate the common midpoints (CMP) fold for each section, which is lower in (b) due to the removal of noisy traces. The top black line represents the surface elevation converted to time. Note increased continuity of the target reflection at 300–400 ms from (a) to (b).

DISCUSSION

The successful imaging of the SS-wavefield in this study confirms that SS-waves were recorded on the HT component. This occurrence is likely a result of complex ground conditions in real-world scenarios, making it challenging to achieve perfectly vertical source signals (Hardage & Wagner, 2014a; Pugin & Yilmaz, 2017). Such conditions hinder optimal source coupling and generate various wavefield components, leading to energy dissipation in horizontal directions (Hardage & Wagner, 2014a, 2014b; Pertuz & Malehmir, 2023b; Pugin & Yilmaz, 2017). Although this energy loss complicates deep imaging of the PP-wavefield, it can be beneficial for analysing the entire wavefield, allowing for higher-resolution information recovery from the same acquisition. The analysed 3C data revealed SS reflections in both HR and HT components, with the HT component consistently showing greater continuity and signal-to-noise ratio. We attribute the higher continuity of SS-wavefield reflections in the HT component to its reduced sensitivity to source-related noise.

Surface waves removal was a significant challenge during SS-wavefield signal processing due to their overlapping propagation velocities and frequencies with SS-wavefield reflections, as well as strong amplitudes. The standard methods used only partially reduced surface wave amplitudes, negatively impacting subsequent coherency-based techniques like RMS velocity analysis and residual static estimation. To address this

18730604, 0, Downloaded from https://onlinelibrary.wiley.com/doi/10.1002/nsg.70010 by Samuel Zappalá - Uppsala Universitet , Wiley Online Library on [08/05/2025]. See the Terms and Conditions (https://onlinelibrary.wiley.com/terms-and-conditions) on Wiley Online Library for rules of use; OA articles are governed by the applicable Creative Commons License

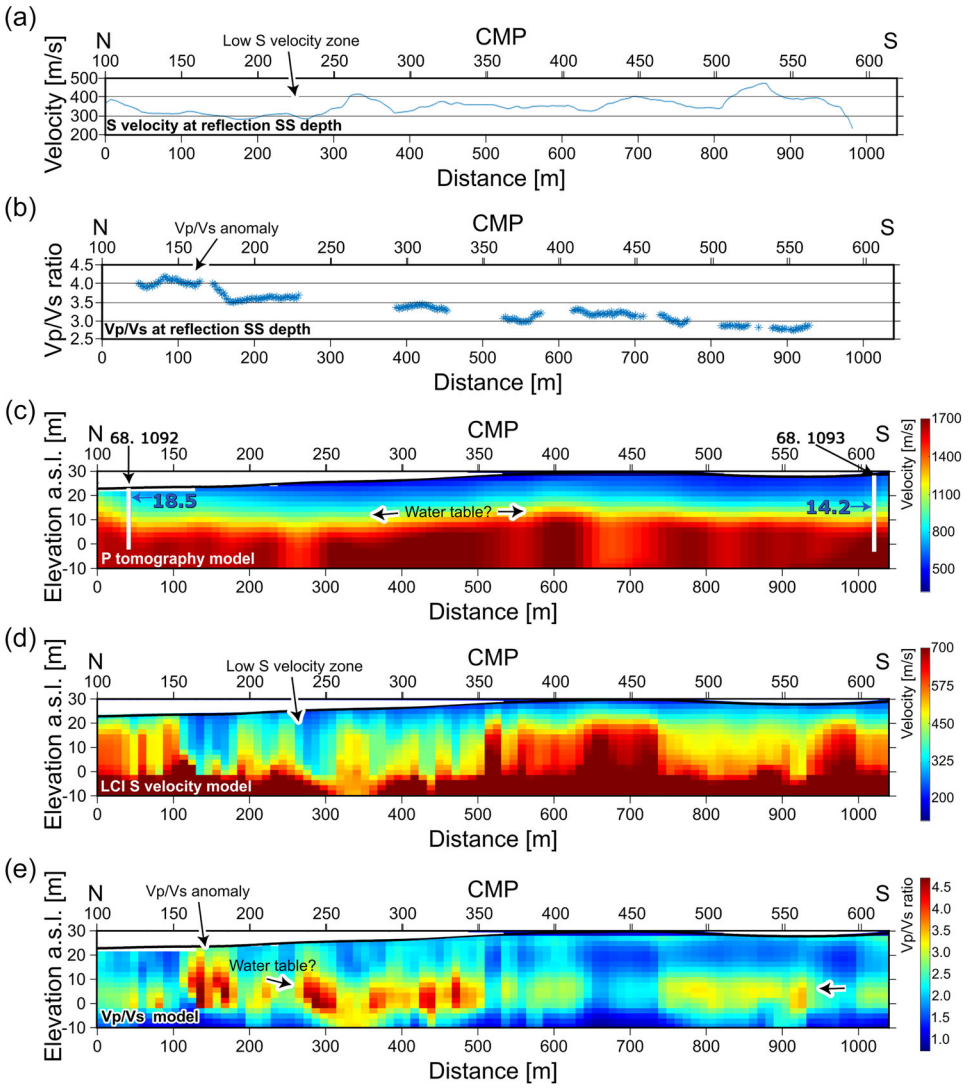

Figure 8 Different velocity estimates at different depths along the profile. (a) Average V_S at the SS-wavefield reflection depth (approximately −20 m elevation) estimated from the best fitting hyperbolas. (b) V_P/V_S ratio at the SS-wavefield reflection depth (approximately −20 m elevation) computed from the SS reflection in the unmigrated PP- and SS-wavefield stacked sections. (c) Portion of the V_P model resulting from first-break traveltime tomography down to −10 m elevation. Boreholes with water table information (Figure 2) are plotted onto the model. (d) V_S model resulting from laterally constrained inversion of the surface wave dispersion curves down to −10 m elevation. (e) V_P/V_S ratio computed from (c) and (d) down to −10 m elevation. CMP, common midpoints.

issue, a manual moveout correction approach is proposed as an alternative to traditional NMO corrections. Conventional NMO relies on estimating velocities to separate desired and unwanted signals; however, when these signals have similar velocities, NMO becomes ineffective. The proposed reflection-picked moveout corrections successfully distinguish between the two wave types due to the increased accuracy of manual picking. This method also compensates for static issues, leading to better alignment of reflections in the CMP gathers and a stronger stacked signal compared to the undesired signal. Applying this method to real data resulted in significant improvements in both CMP gathers and the final SS-wavefield stacked section, enhancing reflection continuity and S/N at the reflection depth (Figure 7).

To ensure effectiveness, a minimum of three points per CMP gather must be picked on the reflection; otherwise, the hyperbola and t_0 estimations will be unreliable. Accuracy improves with more picked traces, stabilizing at a minimum of five in our case. Reason why portions of the stacked section from CMP gathers with fewer than five picks have been excluded from interpretation. Traces where the reflection pick is unclear are likely to degrade the stacked section, and their removal is strongly recommended. As the proposed method estimates the reflection hyperbola based on CMP gathers, it assumes a horizontally layered subsurface, which is valid for the studied area but would require further development, such as integration with dip-moveout corrections, in cases with complex geometries or dipping reflections.

18730604, 0, Downloaded from https://onlinelibrary.wiley.com/doi/10.1002/nsg.70010 by Samuel Zappalá - Uppsala Universitet , Wiley Online Library on [08/05/2025]. See the Terms and Conditions (https://onlinelibrary.wiley.com/terms-and-conditions) on Wiley Online Library for rules of use; OA articles are governed by the applicable Creative Commons License

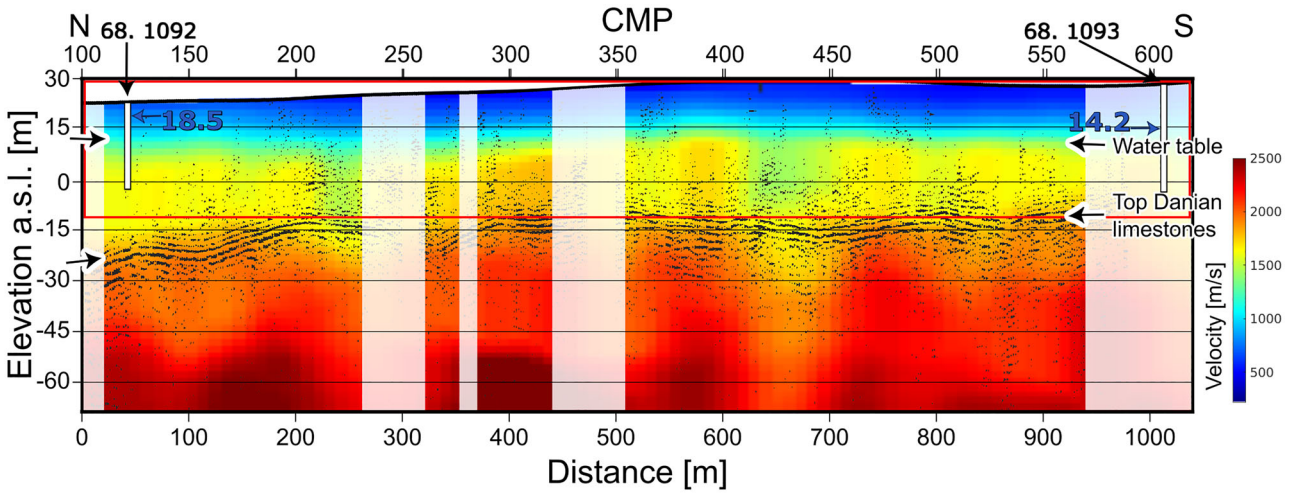

Figure 9 P-wave traveltime tomography (colour values) superimposed to the SS-wavefield unmigrated stacked section converted to depth (black structures). Boreholes with water table information (Figure 2) are plotted onto the section (white bars). The water table (indicated by the colour change in the traveltime tomography) and top of the Danian limestones (stacked section) are indicated by the arrows. The white shaded areas correspond to low Common midpoints (CMP) fold hence excluded in the image. The red rectangle corresponds to the area shown in Figure 8c–e.

Additionally, the proposed correction focuses on a single reflection and does not account for horizontal or vertical variability, leading to inaccurate corrections for shallower or deeper reflections with different velocities. A layer stripping approach could consider multiple reflections but requires further investigation, as it has not yet been tested. The manual picking requirement makes this method time-consuming when analysing large datasets, limiting its applicability mostly to small datasets.

The SS-wavefield unmigrated stacked section converted to depth and the velocity analysis results are jointly interpreted for near-surface characterization. As the computed V_S model is shallower than the reflection imaged in the SS-wavefield stacked section, the P-wave traveltime tomography model is superimposed onto the depth-converted SS-wavefield unmigrated stacked section in Figure 9. The P-wave traveltime tomography model (Figure 8c) shows lower lateral variability with respect to the V_S model (Figure 8d), and thus, the V_P/V_S ratio in the area (Figure 8e) appears to be mostly controlled by the V_S. A strong velocity contrast in the P-wave traveltime tomography model is visible at around 10–15 m elevation. This horizon is not visible in the SS-wavefield stacked section but corresponds in depth to a high V_P/V_S ratio horizon estimated from the velocity models (Figure 8e). This high V_P/V_S ratio value at around 10–15 m elevation is interpreted to represent the water table. When water replaces the air in the pores of the rock structure from the unsaturated shallow zone to the saturated zone below, V_P values are expected to increase due to the higher water velocity with respect to the air velocity. In contrast, V_S is insensitive to the fluid presence due to their zero-shear modulus. The simultaneous increase of V_P and stability of V_S results in an increase of the V_P/V_S ratio (Pasquet et al., 2015) and an absence of SS-wavefield reflections at this depth. This interpretation is further supported by the water table depth as indicated by the available boreholes at around 15 m elevation (borehole numbers 68.1092 and 68.1093 in Figures 2 and 9). The V_P/V_S ratio anomaly between CMP 150 and 200 (Figure 8b,e) is likely due to localized changes in shallow subsurface properties, such as the presence of loose sediments, water saturation, or man-made structures (e.g., excavated materials). Additional data such as GPR measurements for higher resolution imaging and borehole investigations for lithological characterization will be beneficial to identify the nature of this anomaly. Despite resulting from different velocity estimates, the V_P/V_S ratio estimated from the reflections (Figure 8b) shows a similar trend of the subsurface properties as the V_P/V_S ratio estimated from the velocity models (Figure 8e).

The SS-wavefield reflection in the unmigrated stacked section appears undulating and matches the strong velocity contrast visible at around −15 m elevation. Considering the regional studies (Energi Randers Vand A/S, 2007; Miljø- og Fødevareministeriet, 2020; Naturstyrelsen, 2014) and the seismic knowledge of the area (Papadopoulou et al., 2023;Zappalá, Malehmir, Papadopoulou, Gregersen, et al., 2024; Westgate et al., 2025), the reflection pattern is interpreted as a transition zone from the shallowest quaternary sediments (in brown in Figure 2) to the top of the Chalk Group and specifically to the top of the Danian limestones (green in Figure 2). Previous studies show that the top of the Chalk Group is the strongest PP-seismic reflection expected in the study area (Papadopoulou et al., 2023; Westgate et al., 2025; Zappalá, Malehmir, Papadopoulou,

18730604, 0, Downloaded from https://onlinelibrary.wiley.com/doi/10.1002/nsg.70010 by Samuel Zappalá - Uppsala Universitet , Wiley Online Library on [08/05/2025]. See the Terms and Conditions (https://onlinelibrary.wiley.com/terms-and-conditions) on Wiley Online Library for rules of use; OA articles are governed by the applicable Creative Commons License

Gregersen, et al., 2024), and it is likely the same for the SS-wavefield. This transition zone may include the thin pre-quaternary clays (blue in Figure 2) just above the Chalk Group that are expected to have higher discontinuity and a lower impedance contrast (Papadopoulou et al., 2023; Westgate et al., 2025; Zappalá, Malehmir, Papadopoulou, Gregersen, et al., 2024).

Compared to the PP-wavefield stacked section where the imaged reflection appears nearly flat (Figure 4), the SS-wavefield unmigrated stacked section shows higher resolution and is suitable to image finer structures (Figure 7b). This confirms the higher resolution of S-wave imaging with respect to P-wave imaging when similar frequencies are recorded as seen in multiple other studies (Burschil et al., 2015; Carr et al., 1998; Krawczyk, Polom, Beilecke, et al., 2013). We, therefore, conclude that SS-wavefield imaging is more sensitive to the variabilities of the shallow subsurface in this area.

In other S-wave studies, surface waves have been addressed according to local characteristics. When surface waves have lower frequencies than reflections, high-pass filters can be used to remove them (Brodic et al., 2018; Pertuz & Malehmir, 2023a). However, this was not applicable here due to frequency overlap. Another common approach is FK-filtering (Burschil & Buness, 2020), but in this case, the overlap of the two signals prevented surface wave removal without distorting the reflection. Van Zanen (2004) created a method based on the Betti–Rayleigh reciprocity theorem for eliminating love waves, which succeeded on synthetic datasets but was inefficient in real cases. In situations with a high-velocity near-surface layer, surface wave energy may be suppressed, reducing the need for their attenuation (Inazaki, 2004; Polom et al., 2010). In our case, the surface waves were particularly energetic compared to the shallow reflections, likely due to the high source energy (96 kN per each truck) and short offset. Such conditions often occur in datasets aimed at deeper targets, making our method valuable for processing SS-wavefields as a by-product.

For future studies, we recommend implementing an automatic setup for measuring the coordinates of landstreamer recorders, similar to this study. Accurate positioning enhances the reliability of refraction static corrections, improves the efficiency of offset-dependent filters and leads to more precise stacking and better imaging results.

CONCLUSIONS

This work presents a workflow for SS-wavefield reflection imaging using horizontal component data. To address the significant surface wave contamination that hampers accurate NMO corrections of the SS-wavefield data and the large shear statics, we developed a moveout correction based on the desired reflection picks (reflection-picked moveout correction). This approach has proven to be robust and efficient resulting in significant improvements in reflection continuity and details when similar signals need to be separated in the data. The stacked section is complemented with V_P and V_S analysis along with V_P/V_S ratio models to assist shallow subsurface geological interpretation. Our results reveal variabilities in the shallow subsurface and estimate the water table and the top of the Danian limestones (top of the Chalk Group) at approximately 10–15 m and −10 to −20 m elevations, respectively. The quality of the results obtained from the horizontal component underscores the value of multicomponent data acquisitions in providing additional subsurface geological information with affordable and worth additional cost.

ACKNOWLEDGEMENTS

The authors thank the Geological Survey of Denmark and Greenland (GEUS) for financing the seismic survey. We are grateful to numerous students and researchers from Uppsala University, Copenhagen University and LaSalle University who led and supported the field data acquisition. Special thanks to Michael Westgate, Kristina Kucinskaite and Emmanouil Konstantinidis for their effort during the data acquisition and main processing of the data from this site. The authors are grateful to the reviewers and the editors for their valuable comments and contributions, which have contributed to improving the quality of our work.

DATA AVAILABILITY STATEMENT

The data that support the findings of this study are available at https://www.geus.dk/produkter-ydelser-og-faciliteter/data-og-kort/ccs-data-2022-2024.

ORCID

Samuel Zappalá https://orcid.org/0000-0003-3402-6850
Myrto Papadopoulou https://orcid.org/0000-0002-5112-2732
Alireza Malehmir https://orcid.org/0000-0003-1241-2988

REFERENCES

Bharadwaj, P., Drijkoningen, G., Mulder, W., Thorbecke, J., Neducza, B. & Jenneskens, R. (2017) A shear-wave seismic system using full-waveform inversion to look ahead of a tunnel-boring machine. *Near Surface Geophysics*, 15(3), 210–225. Available from: https://doi.org/10.3997/1873-0604.2017014

Brittle, K.F., Lines, L.R. & Dey, A.K. (2001), Vibroseis deconvolution: a comparison of cross-correlation and frequency-domain sweep deconvolution. *Geophysical Prospecting*, 49, 675–686. Available from: https://doi.org/10.1046/j.1365-2478.2001.00291.x

Brodic, B., Malehmir, A., Pugin, A. & Maries, G. (2018) Three-component seismic land streamer study of an esker architecture through S- and surface-wave imaging. *Geophysics*, 83(6), B339–B353. Available from: https://doi.org/10.1190/geo2017-0747.1

18730604, 0, Downloaded from https://onlinelibrary.wiley.com/doi/10.1002/nsg.70010 by Samuel Zappalá - Uppsala Universitet , Wiley Online Library on [08/05/2025]. See the Terms and Conditions (https://onlinelibrary.wiley.com/terms-and-conditions) on Wiley Online Library for rules of use; OA articles are governed by the applicable Creative Commons License

Burschil, T., Beilecke, T. & Krawczyk, C.M. (2015) Finite-difference modelling to evaluate seismic P-wave and shear-wave field data. *Solid Earth*, 6(1), 33–47. Available from: https://doi.org/10.5194/se-6-33-2015

Burschil, T. & Buness, H. (2020) S-wave seismic imaging of near-surface sediments using tailored processing strategies. *Journal of Applied Geophysics*, 173, 103927. Available from: https://doi.org/10.1016/j.jappgeo.2019.103927

Carr, B.J., Hajnal, Z. & Prugger, A. (1998) Shear-wave studies in glacial till. *Geophysics*, 63(4), 1273–1284. Available from: https://doi.org/10.1190/1.1444429

Energi Randers Vand A/S. (2007) Grundvandsmodel for Randers—Opstilling og kalibrering af grundvandsmodel for Randers. *GEUS Grundvandsrapport 91576*. Technical report (Danish). Available from: https://data.geus.dk/grundvandsrapport/detail?id=91576

GeoAtlas. (2024) https://data.geo.dk/geoatlas-live

Hardage, B.A. & Wagner, D. (2014a) Generating direct-S modes with simple, low-cost, widely available seismic sources. *Interpretation*, 2(2), SE1–SE15. Available from: https://doi.org/10.1190/INT-2013-0095.1

Hardage, B.A. & Wagner, D. (2014b) S-S imaging with vertical-force sources. *Interpretation*, 2(2), SE29–SE38. Available from: https://doi.org/10.1190/INT-2013-0097.1

Hardage, R. (2015) Simplifying and lowering the cost of S-wave reflection seismology through use of P-wave sources. *SEG-GSH Webinar*.

Hardage, B. (2017) Practicing S-wave reflection seismology with "P-wave" sources: concepts, principles, and overview. In: *SEG Technical Program Expanded Abstracts* 2017, Houston, TX, SEG. pp. 5152–5156. Available from: https://doi.org/10.1190/segam2017-17256173.1

Inazaki, T. (2004) High-resolution seismic reflection surveying at paved areas using an S-wave type Land Streamer. *Exploration Geophysics*, 35(1), 1–6. Available from: https://doi.org/10.1071/EG04001

Kearey, P., Brooks, M., Hill, I. (2002) *An introduction to geophysical exploration*, 3rd edition, Hoboken, NJ: Blackwell Science.

Krawczyk, C.M., Polom, U. & Beilecke, T. (2013) Shear-wave reflection seismics as a valuable tool for near-surface urban applications. *The Leading Edge*, 32(3), 256–263. Available from: https://doi.org/10.1190/tle32030256.1

Krawczyk, C.M., Polom, U., Malehmir, A. & Bastani, M. (2013) Quick-clay landslides in Sweden-insights from shear-wave reflection seismics and geotechnical integration. In: *Near Surface Geoscience 2013—19th EAGE European Meeting of Environmental and Engineering Geophysics*, Utrecht, European Association of Geoscientists & Engineers. Available from: https://doi.org/10.3997/2214-4609.20131348

Lieberkind, K., Bang, I., Mikkelsen, N. & Nygaard, E. (1982) Late cretaceous and Danian limestone. *Danmarks Geologiske Undersøgelse Serie B*, 8(25), 49–62. Available from: https://doi.org/10.34194/serieb.v8.7069

Macrides, C.G. & Kelamis, P.G. (2000) A 9C-2D land seismic experiment for lithology estimation of a permian clastic reservoir. *GeoArabia*, 5(3), 427–440. Available from: https://doi.org/10.2113/geoarabia0503427

Malehmir, A., Hong, T.K., Lee, J., Zappalá, S., Brodic, B., Chung, D. et al. (2022) Fault intersections control short period intraplate start-stop seismicity in the Korean Peninsula. *Tectonophysics*, 834, 229387. Available from: https://doi.org/10.1016/j.tecto.2022.229387

Malehmir, A., Socco, L.V., Bastani, M., Krawczyk, C.M., Pfaffhuber, A.A., Miller, R.D. et al. (2016) Near-surface geophysical characterization of areas prone to natural hazards: a review of the current and perspective on the future. *Advances in Geophysics*, 57, 51–146. Available from: https://doi.org/10.1016/bs.agph.2016.08.001

Miljø- og Fødevareministeriet. (2020) Grundvandskortlægning for Randers Kommune -*Kortlægning i Randers kommune*. Miljø- og Fødevareministeriet - *GEUS Grundvandsrapport 94521*. Technical report (Danish). Available from: https://data.geus.dk/grundvandsrapport/detail?id=94521

Miller, G. & Pursey, H. (1954) The field and radiation impedance of mechanical radiators on the free surface of a semi-infinite isotropic solid. *Proceedings of the Royal Society of London. Series A. Mathematical and Physical Sciences*, 223(1155), 521–541. Available from: https://doi.org/10.1098/rspa.1954.0134

Naturstyrelsen. (2014) *Grundvandsmodel for Randers nord kortlægninsområde*. *GEUS Grundvandsmodel 90893*. Technical report (Danish). Available from: https://data.geus.dk/grundvandsrapport/detail?id=90893

Papadopoulou, M., Colombero, C., Staring, M., Singer, J., Eddies, R., Fliedner, M. et al. (2021) Fast near-surface investigation with surface-wave attributes. In *NSG2021 2nd Conference on Geophysics for Infrastructure Planning, Monitoring and BIM*. Utrecht, European Association of Geoscientists & Engineers. pp. 1–5. Available from: https://doi.org/10.3997/2214-4609.202120128

Papadopoulou, M., Zappalá, S., Malehmir, A., Gregersen, U., Hjelm, L., Nielsen, L. et al. (2023) Innovating land seismic investigations for CO2 geologic storage in Denmark. *Geophysics*, 88(5), 1–57. Available from: https://doi.org/10.1190/geo2022-0693.1

Pasquet, S., Bodet, L., Dhemaied, A., Mouhri, A., Vitale, Q., Rejiba, F. et al. (2015) Detecting different water table levels in a shallow aquifer with combined P-, surface and SH-wave surveys: insights from VP/VS or Poisson's ratios. *Journal of Applied Geophysics*, 113, 38–50. Available from: https://doi.org/10.1016/j.jappgeo.2014.12.005

Pertuz, T. & Malehmir, A. (2023a) Ultrahigh-resolution 9C seismic survey in a landslide prone area in southwest of Sweden. *Geophysical Journal International*, 235(3), 2094–2106. Available from: https://doi.org/10.1093/gji/ggad346

Pertuz, T. & Malehmir, A. (2023b) Ultrahigh-resolution shear-wave reflection imaging of vertical-component data in a quick-clay prone to landslide area in southwest Sweden. *Geophysics*, 88(3), B121–B133. Available from: https://doi.org/10.1190/geo2021-0832.1

Polom, U., Hansen, L., Sauvin, G., L'Heureux, J.-S., Lecomte, I., Krawczyk, C.M. et al. (2010) 18. High-resolution SH-wave seismic reflection for characterization of onshore ground conditions in the Trondheim Harbor, Central Norway. In: Advances in *near-surface seismology and ground-penetrating radar*. Houston, TX, Society of Exploration Geophysicists, American Geophysical Union, Environmental and Engineering Geophysical Society. pp. 297–312. Available from: https://doi.org/10.1190/1.9781560802259.ch18

Pugin, A.J.-M., Pullan, S.E. & Hunter, J.A. (2009) Multicomponent high-resolution seismic reflection profiling. *The Leading Edge*, 28(10), 1248–1261. Available from: https://doi.org/10.1190/1.3249782

Pugin, A.J.-M., Pullan, S.E. & Hunter, J.A. (2013) Shear-wave high-resolution seismic reflection in Ottawa and Quebec City, Canada. *The Leading Edge*, 32(3), 250–255. Available from: https://doi.org/10.1190/tle32030250.1

Pugin, A.J.M. & Yilmaz, O. (2017) There is no pure P- or S-wave land seismic source. In: *SEG Technical Program Expanded Abstracts*. Houston, TX, SEG. pp. 5162–5166. Available from: https://doi.org/10.1190/segam2017-17650931.1

Pugin, A. & Yilmaz, Ö. (2019) Optimum source-receiver orientations to capture PP, PS, SP, and SS reflected wave modes. *The Leading Edge*, 38(1), 45–52. Available from: https://doi.org/10.1190/tle38010045.1

Socco, L.V., Boiero, D., Foti, S. & Wisén, R. (2009) Laterally constrained inversion of ground roll from seismic reflection records. *Geophysics*, 74(6), G35–G45. Available from: https://doi.org/10.1190/1.3223636

Socco, L.V., Comina, C. & Khosro Anjom, F. (2017) Time-average velocity estimation through surface-wave analysis: part 1—S-wave velocity. *Geophysics*, 82(3), U49–U59. Available from: https://doi.org/10.1190/geo2016-0367.1

18730604, 0, Downloaded from https://onlinelibrary.wiley.com/doi/10.1002/nsg.70010 by Samuel Zappalá - Uppsala Universitet , Wiley Online Library on [08/05/2025]. See the Terms and Conditions (https://onlinelibrary.wiley.com/terms-and-conditions) on Wiley Online Library for rules of use; OA articles are governed by the applicable Creative Commons License

Surlyk, F., Damholt, T. & Bjerager, M. (2006) Stevns Klint, Denmark: uppermost Maastrichtian chalk, Cretaceous–Tertiary boundary, and lower Danian bryozoan mound complex. *Bulletin of the Geological Society of Denmark*, 54, 1–48. Available from: https://doi.org/10.37570/bgsd-2006-54-01

Tryggvason, A., Rögnvaldsson, S.T. & Flóvenz, G. (2002) Three-dimensional imaging of the P-and S-wave velocity structure and earthquake locations beneath Southwest Iceland. *Geophysical Journal International*, 151(3), 848–866. Available from: https://doi.org/10.1046/j.1365-246X.2002.01812.x

Van Zanen, L.S. (2004) Removing love waves from shallow seismic SH-wave data. PhD Thesis. Delft: TU Delft. https://resolver.tudelft.nl/uuid:d467c131-3e61-47b1-809a-3b15f69b7765

Wadas, S.H., Polom, U. & Krawczyk, C.M. (2016) High-resolution shear-wave seismic reflection as a tool to image near-surface subrosion structures—a case study in Bad Frankenhausen, Germany. *Solid Earth*, 7(5), 1491–1508. Available from: https://doi.org/10.5194/se-7-1491-2016

Westgate, M., Kucinskaite, K., Konstantinidis, E., Malehmir, A., Papadopoulou, M., Gregersen, U. et al. (2025) Seismic imaging of halokinetic sequences and structures with high-resolution, dual-element acquisition, and processing: applications to the gassum structure in Eastern Jutland, Denmark. *Earth and Space Science*, 12(1), e2024EA004014. Available from: https://doi.org/10.1029/2024EA004014

Yilmaz, Ö. (2021) *Land seismic case studies for near-surface modeling and subsurface imaging*. Houston, TX: Society of Exploration Geophysicists. Available from: https://doi.org/10.1190/1.9781560803812

Zappalá, S., Malehmir, A., Papadopoulou, M., Gregersen, U., Funck, T., Clausen, O.R. et al. (2024) Combined onshore and offshore wide scale seismic data acquisition and imaging for CCS exploration in Havnsø, Denmark. *Geophysics*, 89(4), B257–B272. Available from: https://doi.org/10.1190/geo2023-0503.1

Zappalà, S., Malehmir, A., Papadopoulou, M., Westgate, M., Putnaite, J., Markovic, M. et al. (2024) Reflection seismic acquisition for onshore CCS applications in Denmark—an overview. In: *Fifth EAGE Global Energy Transition Conference & Exhibition (GET 2024)*. Utrecht, European Association of Geoscientists & Engineers. pp. 1–5. Available from: https://doi.org/10.3997/2214-4609.202421062

How to cite this article: Zappalá, S., Papadopoulou, M. & Malehmir, A. (2025) Shear-wave tailored moveout corrections to improve multicomponent reflection seismic imaging. *Near Surface Geophysics*, 00–00. https://doi.org/10.1002/nsg.70010

18730604, 0, Downloaded from https://onlinelibrary.wiley.com/doi/10.1002/nsg.70010 by Samuel Zappalá - Uppsala Universitet , Wiley Online Library on [08/05/2025]. See the Terms and Conditions (https://onlinelibrary.wiley.com/terms-and-conditions) on Wiley Online Library for rules of use; OA articles are governed by the applicable Creative Commons License